Fisher's Linear Spectral Mixture Analysis

Chein-I Chang, *Senior Member, IEEE*, and Baohong Ji, *Student Member, IEEE*

***Abstract*—Linear spectral mixture analysis (LSMA) has been widely used in subpixel analysis and mixed-pixel classification. One commonly used approach is based on either the least square error (LSE) criterion such as least squares LSMA or the signal-to-noise ratio (SNR) such as orthogonal subspace projection (OSP). Unfortunately, it is known that such criteria are not necessarily optimal for pattern classification. This paper presents a new and alternative approach to LSMA, called Fisher's LSMA (FLSMA). It extends the well-known pure-pixel-based Fisher's linear discriminant analysis to LSMA. Interestingly, what can be done for the LSMA can be also developed for the FLSMA. Of particular interest are two types of constraints imposed on the LSMA, target signature-constrained LSMA and target abundance-constrained LSMA, which can be also derived in parallel for the FLSMA, to be called feature-vector-constrained FLSMA (FVC-FLSMA) and abundance-constrained FLSMA (AC-FLSMA), respectively. Since Fisher's ratio used by the FLSMA is a more appropriate classification criterion than the LSE or SNR used for the LSMA, the FVC-FLSMA improves over the classical least squares based LSMA and SNR-based OSP in mixed-pixel classification. Similarly, the AC-FLSMA also improves abundance-constrained least squares based LSMA in quantification of abundance fractions.**

***Index Terms*—Abundance-constrained Fisher's linear spectral mixture analysis (AC-FLSMA), feature-vector-constrained Fisher's linear spectral mixture analysis (FVC-FLSMA), Fisher's linear discriminant analysis (FLDA), Fisher's linear spectral mixture analysis (FLSMA), linearly constrained discriminant analysis (LCDA), mixed-pixel classification.**

NOMENCLATURE

AC-FLSMA	Abundance-constrained FLSMA.
AFCLS-FLSMA	Abundance fully constrained least squares FLSMA.
ANC	Abundance nonnegativity constraint.
ASC	Abundance sum-to-one constraint.
CEM	Constrained energy minimization.
FCLS	Fully constrained least squares.
FVC-FLSMA	Feature-vector-constrained FLSMA.
FLDA	Fisher's linear discriminant analysis.
FLSMA	Fisher's LSMA.
LCDA	Linearly constrained discriminant analysis.
LCMV	Linearly constrained minimum variance.
LSMA	Linear spectral mixture analysis.
OSP	Orthogonal subspace projection.
LSOSP	Least squares orthogonal subspace projection (*a posteriori* OSP).
RMFD	Correlation matched filter-based distance.
TCIMF	Target-constrained interference-minimized filter.

Manuscript received August 21, 2004; revised October 30, 2005.

C.-I Chang is with the Remote Sensing Signal and Image Processing Laboratory, Department of Computer Science and Electrical Engineering, University of Maryland, Baltimore County, Baltimore, MD 21250 USA and also with the Department of Electrical Engineering, National Chung Hsing University, Taichung 402, Taiwan, R.O.C. (e-mail: cchang@umbc.edu).

B. Ji is with the Remote Sensing Signal and Image Processing Laboratory, Department of Computer Science and Electrical Engineering, University of Maryland, Baltimore County, Baltimore, MD 21250 USA.

Digital Object Identifier 10.1109/TGRS.2006.872085

I. INTRODUCTION

TWO major issues of interest in remote-sensing image processing but never encountered in the traditional two-dimensional (2-D) image processing or three-dimensional (3-D) video processing are subpixels and mixed pixels. Due to the use of spectral channels in various wavelengths, an image pixel is actually a pixel vector, of which each component is a single pixel in an image acquired by a particular spectral channel. As a result, it is often the case that different substances can be diagnosed by their spectral properties in a single pixel vector. Such a substance may appear in either at subpixel scale or a form mixed by other substances in a pixel vector. In order to perform data analysis caused by subpixels and mixed pixels, pure-pixel-based traditional image processing may not be directly applicable or effective. Instead, a common approach, referred to as LSMA or linear spectral unmixing, is generally used for this purpose [1]–[3]. It models an image pixel vector as an admixture linearly mixed by substances that are assumed to be present in the pixel vector. Accordingly, the LSMA actually performs abundance-fraction estimation for each substance in a pixel vector so as to achieve classification, which is opposed to the class-map labeling process performed by pure-pixel-based image processing.

Many algorithms have been developed for the LSMA in subpixel analysis [3], [4] and mixed-pixel classification [1]–[3], [5]–[13]. Despite that it has been shown in [10]–[13] that constrained LSMA actually produced better results than unconstrained LSMA in abundance estimation, the LSMA is generally preferred and implemented as unconstrained spectral unmixing. This is because the constrained LSMA cannot be solved analytically and must rely on numerical solutions [10]–[13], compared to the unconstrained LSMA that has closed-form solutions, such as least squares based LSMA approaches [3], [5]–[9], signal-to-noise ratio (SNR)-based OSP [6]–[9], and Mahalanobis distance-based Gaussain maximum likelihood estimation (GMLE) [7]. These approaches to unconstrained LSMA are second-order statistics-based techniques and arrive at the same matched filter [3]. Consequently, they can be considered least square error (LSE)-based approaches. However, according to Juang and Katagiri [14], the LSE is not necessarily the best criterion to measure classification error. It is known that the FLDA is one of the major methods widely used in pattern classification [15]. It makes use of the so-called Fisher's ratio, the ratio of between-class scatter matrix to within-class scatter matrix, as a criterion to generate a set of feature vectors that can constitute a feature space for better classification. Since the FLDA-generated feature vectors are not necessarily orthogonal, an alternative approach to FLDA

was developed by Soltanian-Zadeh *et al.* [16], where Fisher's ratio was replaced with the ratio of interdistance to intradistance so that its generated feature vectors could be aligned along mutual orthogonal directions. This approach was shown to be successful in magnetic resonance (MR) image classification. Recently, the approach of Soltanian-Zadeh *et al.* was further extended to LCDA by Du and Chang for hyperspectral image classification to improve LSMA classification [17]. Technically speaking, the feature vectors obtained in [16] and [17] are not Fisher's feature vectors because the interdistance to intradistance ratio of Soltanian-Zadeh *et al.*'s is not Fisher's ratio. Second, the feature vectors were not designed for mixed-pixel classification. In principle, the FLDA is a pure-pixel-based class-labeling technique where the clustering procedure is performed based on interpixel spatial correlation among data samples. Therefore, when it is applied to remote-sensing images, it was implemented in a simple and straightforward manner on a pure-pixel basis. Consequently, the FLDA produces a class-labeled map that is different from grayscale fractional-abundance maps generated by the LSMA.

This paper revisits the FLDA and presents a new approach, referred to as FLSMA, which can be considered as a mixed-pixel classification version of the FLDA. It directly extends the FLDA to perform subpixel detection and mixed-pixel classification rather than pure-pixel classification. Therefore, an immediate benefit from such extension is subpixel detection, which cannot be accomplished by the FLDA. Additionally, like other mixed-pixel classification techniques, the FLSMA can also produce grayscale fractional-abundance maps for each of classes to be classified. In particular, two types of constraints imposed on the LSMA, target signature-constrained mixed-pixel classification [3], [18] and target abundance-constrained mixed-pixel classification, discussed in [3] and [10]–[13], can be also derived for the FLSMA. In the LSMA, the former constrains target signatures of interest along desired directions to derive an LCMV approach [3], [18], [19], which includes the CEM [20] as its special case [3], [18]. The latter implements ASC and ANC to derive three least squares abundance-constrained LSMA approaches, called sum-to-one constrained least squares (SCLS), nonnegativity constrained least squares (NCLS), and FCLS [10], [13]. Interestingly, these two types of constrained approaches can be also developed for the FLSMA. One is called FVC-FLSMA, similar to constraints imposed on target signatures. It constrains the FLDA in the sense that the generated Fisher's feature vectors are aligned along mutual orthogonal directions in the same way that both approaches by Soltanian-Zadeh *et al.* and the LCDA do for their interdistance to intradistance ratio-generated feature vectors. The classifier resulting from the FVC-FLSMA operates a similar functional form to that implemented by the LCMV classifier except two crucial differences. One is that the FVC-FLSMA replaces the sample correlation matrix used in the LCMV classifier with the within-class scatter matrix. A second difference is that the FVC-FLSMA classifier is actually a mixed-pixel classification technique using Fisher's ratio as a classification measure as opposed to the LCMV classifier, which uses the LSE as a classification criterion. Therefore, as expected, the FVC-FLSMA generally performs better than the LCMV in mixed-pixel classification. A second type of constrained approaches that can be derived from the FLSMA is called AC-FLSMA, which imposes constraints on abundance fractions of feature vectors instead of feature-vector directions. The AC-FLSMA implements Fisher's ratio as a criterion for optimality to carry out mixed-pixel classification while using the LSE to perform abundance-fraction estimation. Accordingly, three types of AC-FLSMA can be further derived, called abundance sum-to-one constrained-FLSMA (ASCLS-FLSMA), abundance nonnegativity constrained least squares FLSMA (ANCLS-FLSMA), and AFCLS-FLSMA. According to our conducted experiments the AC-FLSMA generally estimates abundance fractions more accurately than its counterpart constrained LSMA.

The remainder of this paper is organized as follows. Section II develops a feature-vector-constrained FLDA approach that constrains the FLDA-generated feature vectors along with mutual orthogonal directions. Section III considers an AC-FLSMA that imposes abundance constraints on the FLDA-generated vectors in the least squares sense. Section IV presents experiments to conduct a comparative performance between the FLSMA and other LSMA-based methods. Finally, Section V concludes some remarks and summarizes the contributions.

II. FVC-FLSMA

The FLDA is one of the most widely used pattern classification techniques in pattern recognition [15]. An application of the FLDA to hyperspectral image classification was also explored in [3], [16], and [17]. Its strength in pattern classification lies on the criterion used for optimality, which is called Fisher's ratio, defined by the ratio of between-class scatter matrix to within-class scatter matrix.

More specifically, assume that there are n training sample vectors $\{\mathbf{r}_i\}_{i=1}^{n}$ for p-class classification, $C_1, C_2, \ldots, C_p$, with n_j being the number of training sample vectors in the jth class C_j. Let $\boldsymbol{\mu}$ be the global mean of the entire training sample vectors, denoted by $\boldsymbol{\mu} = (1/n)\sum_{i=1}^{n} \mathbf{r}_i$, and let $\boldsymbol{\mu}_j$ be the mean of the training sample vectors in the jth class C_j, denoted by $\boldsymbol{\mu}_j = (1/n_j)\sum_{\mathbf{r}_i \in C_j} \mathbf{r}_i$. The within-class scatter matrix $\mathbf{S}_{\mathrm{W}}$, between-class scatter matrix $\mathbf{S}_{\mathrm{B}}$, and total scatter matrix are defined in [15] as follows:

$$\mathbf{S}_{\mathrm{W}} = \sum_{j=1}^{p} \mathbf{S}_j, \qquad \text{where } \mathbf{S}_j = \sum_{\mathbf{r} \in C_j} (\mathbf{r} - \boldsymbol{\mu}_j)(\mathbf{r} - \boldsymbol{\mu}_j)^{\mathrm{T}} \quad (1)$$

$$\mathbf{S}_{\mathrm{B}} = \sum_{j=1}^{p} n_j (\boldsymbol{\mu}_j - \boldsymbol{\mu})(\boldsymbol{\mu}_j - \boldsymbol{\mu})^{\mathrm{T}} \quad (2)$$

$$\mathbf{S}_{\mathrm{T}} = \sum_{i=1}^{n} (\mathbf{r}_i - \boldsymbol{\mu})(\mathbf{r}_i - \boldsymbol{\mu})^{\mathrm{T}} = \mathbf{S}_{\mathrm{W}} + \mathbf{S}_{\mathrm{B}}. \quad (3)$$

By virtue of (1) and (2), Fisher's ratio (also known as Rayleigh's quotient [15]) is then defined by

$$\frac{\mathbf{x}^{\mathrm{T}} \mathbf{S}_{\mathrm{B}} \mathbf{x}}{\mathbf{x}^{\mathrm{T}} \mathbf{S}_{\mathrm{W}} \mathbf{x}} \text{ over vector } \mathbf{x}. \quad (4)$$

The goal of the FLDA is to find a set of feature vectors that maximize Fisher's ratio specified by (4). The number of feature vectors found by Fisher's ratio is determined by the number of classes p to be classified, which is $p - 1$.

In this section, we extend the FLDA to perform mixed-pixel classification in the sense of Fisher's ratio. One difficulty in doing so is that the FLDA-generated feature vectors are not

image endmembers commonly used in the LSMA. Instead, they are discriminant vectors that are used to determine decision boundaries among classes. Therefore, the number of feature vectors generated by the FLDA is $p-1$, which is one less than the number of image endmembers p assumed to be present in the image data. The FLDA finds a set of feature vectors via (4) by solving a generalized eigenvalue problem specified by

$$\mathbf{S}_{\mathrm{W}}^{-1}\mathbf{S}_{\mathrm{B}}\mathbf{w}=\eta\mathbf{w} \tag{5}$$

where η is a generalized eigenvalue. Since the rank of the between-class scatter matrix $\mathbf{S}_{\mathrm{B}}$ is only $p-1$, there are only $p-1$ nonzero eigenvalues associated with (5).

However, in order to implement the FLDA as an LSMA technique, we need p feature vectors that can be used to serve as image endmembers rather than discriminant vectors generated by (5). One way to mitigate this dilemma was proposed by Soltanian-Zadeh *et al.* [16] and Du and Chang [17], who replaced Fisher's ratio with the ratio of interdistance to intradistance while constraining the class means along mutual orthogonal directions. As a consequence, the interdistance was shown to be constant and could be removed from the criterion, which only involves the within-class scatter matrix $\mathbf{S}_{\mathrm{W}}$. In this case, these class means can be used to represent the desired image endmembers for the LSMA rather than discriminant vectors and the within-class scatter matrix $\mathbf{S}_{\mathrm{W}}$ describes the variance centered at each of the image endmembers. In spite of their success in MR image classification and hyperspectral image classification, their used criterion was not really Fisher's ratio. Therefore, they cannot be considered as FLDA-based approaches. In this section, we present a Fisher-ratio-based LSMA approach, to be called FVC-FLSMA, which directly extends the FLDA in a similar manner that was derived in [17], where its derived Fisher's feature vectors are also mutually orthogonal. As a consequence, Du–Chang's developed LCDA can be shown equivalent to the FVC-FLSMA. Because the derivations for the FVC-LSMA are relatively tedious, their mathematical details are provided in the Appendix, and only the results that will be needed for subsequent discussions are summarized as follows.

Let $\mathbf{w}_l$ be the lth feature vector that maximizes Fisher's ratio subject to the constraint that the lth feature vector must be aligned with the lth class-mean vector $\boldsymbol{\mu}_l$, but also orthogonal to other feature vectors $\{\boldsymbol{\mu}_k\}_{k=1,k\neq l}^{p}$. The FVC-FLSMA problem can be cast by solving

$$\max_{\mathbf{w}_l}\left\{\frac{\mathbf{w}_l^{\mathrm{T}}\mathbf{S}_{\mathrm{B}}\mathbf{w}_l}{\mathbf{w}_l^{\mathrm{T}}\mathbf{S}_{\mathrm{W}}\mathbf{w}_l}\right\} \text{ subject to the constraint that } \mathbf{w}_l^{\mathrm{T}}\boldsymbol{\mu}_j=\delta_{lj},\qquad \text{for } 1\le j\le p. \tag{6}$$

Assume that $\mathbf{r}$ is an L-dimensional pixel column vector and $\mathbf{M}=\lfloor\boldsymbol{\mu}_1\boldsymbol{\mu}_2\ldots\boldsymbol{\mu}_p\rfloor$ is the class-mean matrix. As shown in the Appendix, the lth feature vector produced by the FVC-LSMA $\mathbf{w}_l^{\mathrm{FVC-FLSMA}}$ is given by (A10) where $\mathbf{1}_l$ is the lth p-dimensional unit vector specified by $\mathbf{1}_l=(0,\ldots,0,\underbrace{1}_{l},0,\ldots,0)^{\mathrm{T}}$.

Operating the $\mathbf{w}_l^{\mathrm{FVC-FLSMA}}$ on the image pixel vector $\mathbf{r}$ yields the abundance fraction of the lth class mean $\boldsymbol{\mu}_l$, which is α_l, given by

$$\alpha_l=\left(\mathbf{w}_l^{\mathrm{FVC-FLSMA}}\right)^{\mathrm{T}}\mathbf{r}. \tag{7}$$

Furthermore, if we define a weight matrix $\mathbf{W}^{\mathrm{FVC-FLSMA}}=[\mathbf{w}_1^{\mathrm{FVC-FLSMA}}\ \mathbf{w}_2^{\mathrm{FVC-FLSMA}}\ \cdots\ \mathbf{w}_p^{\mathrm{FVC-FLSMA}}]$ formed by the p FVC-FLSMA-generated feature vectors, we can obtain the FVC-FLSMA solution in a matrix form, given by (A14) (see the Appendix). Applying (A14) to the image pixel vector $\mathbf{r}$ results in the abundance-fraction vector α of the p-dimensional class-mean vector present in $\mathbf{r}$, which can be estimated by (A15) with $\boldsymbol{\alpha}(\mathbf{r})=(\alpha_1(\mathbf{r}),\alpha_2(\mathbf{r}),\ldots,\alpha_p(\mathbf{r}))^{\mathrm{T}}$ and $\alpha_l(\mathbf{r})$ obtained by (7). Here, we include $\mathbf{r}$ in the notations to indicate the dependence of the abundance fractions on the pixel vector $\mathbf{r}$.

Since the FVC-LSMA uses (7) to perform mixed-pixel classification, it produces a fractional-abundance image for each of the classes for classification as does any other mixed-pixel classification technique. The only difference is that the image endmembers used in the LSMA are now replaced by the class-mean vectors $\{\boldsymbol{\mu}_k\}_{k=1}^{p}$. Therefore, the FVC-generated fractional-abundance images generally require a threshold method such as the one in [3] to calculate classification rates.

A. Relationship Between FVC-FLSMA and LCMV, TCIMF, and CEM

Recalling the LCMV classifier in [3] and [18], its weight matrix ([3, eq. (11.16)] or [18, eq. (6)]) is given by

$$\begin{aligned}\mathbf{W}^{\mathrm{LCMV}}&=\mathbf{R}_{L\times L}^{-1}\mathbf{M}\left(\mathbf{M}^{\mathrm{T}}\mathbf{R}_{L\times L}^{-1}\mathbf{M}\right)^{-\mathrm{T}}\mathbf{C}\\&=\mathbf{R}_{L\times L}^{-1}\mathbf{M}\left(\mathbf{M}^{\mathrm{T}}\mathbf{R}_{L\times L}^{-1}\mathbf{M}\right)^{-1}\mathbf{C}\end{aligned} \tag{8}$$

where the matrix $\mathbf{C}$ is the constraint matrix and $\mathbf{R}_{L\times L}$ is the data correlation matrix.

Now, let $\mathbf{I}_{p\times p}$ be the $p\times p$ identity matrix. Multiplying $\mathbf{I}_{p\times p}$ on the right of (A15), we can rewrite (A15) as

$$\begin{aligned}\mathbf{W}^{\mathrm{FVC-FLSMA}}&=\mathbf{W}^{\mathrm{FVC-FLSMA}}\mathbf{I}_{p\times p}\\&=\mathbf{S}_{\mathrm{W}}^{-1}\mathbf{M}\left(\mathbf{M}^{\mathrm{T}}\mathbf{S}_{\mathrm{W}}^{-1}\mathbf{M}\right)^{-1}\mathbf{I}_{p\times p}.\end{aligned} \tag{9}$$

Comparing (9) against the LCMV-generated weight matrix specified by (8), an immediate finding is that the FVC-FLSMA-generated weight matrix given by (9) has the same form as does (8), where the within-class scatter matrix $\mathbf{S}_{\mathrm{W}}$ and the identity matrix $\mathbf{I}_{p\times p}$ used by the FVC-LSMA in (9) correspond to the sample spectral correlation matrix $\mathbf{R}_{L\times L}$ and the constraint matrix $\mathbf{C}$ used by the LCMV in (8), respectively. The constraint matrix $\mathbf{I}_{p\times p}$ in (9) is exactly the same p constraints $\mathbf{w}_l^{\mathrm{T}}\boldsymbol{\mu}_j=\delta_{lj}$ used in (6). Similarly, when the constraint matrix $\mathbf{I}_{p\times p}$ in (9) is replaced by a constraint vector, the lth p-dimensional unit vector $\mathbf{1}_l$, the resulting weighting matrix $\mathbf{W}^{\mathrm{FVC-FLSMA}}$ becomes a weighting vector given by (A10), which corresponds to the TCIMF [3], [18], [19] with the within-class scatter matrix $\mathbf{S}_{\mathrm{W}}$ in (9) replaced by $\mathbf{R}_{L\times L}$. If there is only a desired target signature $\mathbf{d}$ constrained by $\mathbf{d}^{\mathrm{T}}\mathbf{w}=1$ via (6), (9) turns out to be the same functional form implemented by the CEM in [3] and [18]–[20], where the within-class scatter matrix $\mathbf{S}_{\mathrm{W}}$ and $\boldsymbol{\mu}_l$ are replaced by the sample correlation matrix $\mathbf{R}_{L\times L}$ and $\mathbf{d}$, respectively.

B. Relationship Between FVC-FLSMA and OSP

In analogy with the LCMV, we replace $\mathbf{S}_{\mathrm{W}}^{-1}$ in (A10) with $P_{\mathbf{U}}^{\perp}$, defined by

$$P_{\mathbf{U}}^{\perp}=\mathbf{I}-\mathbf{U}(\mathbf{U}^{\mathrm{T}}\mathbf{U})^{-1}\mathbf{U}^{\mathrm{T}} \tag{10}$$

where $\mathbf{U} = [\boldsymbol{\mu}_1 \cdots \boldsymbol{\mu}_{l-1}\boldsymbol{\mu}_{l+1} \cdots \boldsymbol{\mu}_p]$. The weighting vector $\mathbf{w}_l^{\mathrm{FVC-FRLSMA}}$ resulting from replacing $\mathbf{S}_{\mathrm{W}}^{-1}$ in (A10) with $P_{\mathbf{U}}^{\perp}$ in (10) becomes the LSOSP in [3] and [9]

$$\mathbf{w}_l^{\mathrm{LSOSP}} = P_{\mathbf{U}}^{\perp}\mathbf{M}\left(\mathbf{M}^{\mathrm{T}}P_{\mathbf{U}}^{\perp}\mathbf{M}\right)^{-1}\mathbf{1}_l. \tag{11}$$

With this interpretation, the FVC-FLSMA can be considered as an FLDA version of the OSP.

Additionally, we can define a linear transformation by $\hat{\mathbf{r}} = P_{\mathbf{U}}^{\perp}\mathbf{r}$ and $\hat{\mathbf{M}} = P_{\mathbf{U}}^{\perp}\mathbf{M}$ for an image pixel vector $\mathbf{r}$. The resulting image with pixel vectors described by $\hat{\mathbf{r}}$ is called the $P_{\mathbf{U}}^{\perp}$-whitened hyperspectral image. Let $\hat{\boldsymbol{\mu}}_l$ be the $P_{\mathbf{U}}^{\perp}$-whitened lth class mean defined by $\hat{\boldsymbol{\mu}}_l = P_{\mathbf{U}}^{\perp}\boldsymbol{\mu}_l$. Equation (11) is then reduced to

$$\mathbf{w}_l^{\mathrm{LSOSP}} = \hat{\mathbf{M}}\left(\hat{\mathbf{M}}^{\mathrm{T}}\hat{\mathbf{M}}\right)^{-1}\mathbf{1}_l = \left(\hat{\boldsymbol{\mu}}_l^{\mathrm{T}}P_{\hat{\mathbf{U}}}^{\perp}\hat{\boldsymbol{\mu}}_l\right)^{-1}P_{\hat{\mathbf{U}}}^{\perp}\hat{\boldsymbol{\mu}}_l \tag{12}$$

where $\hat{\mathbf{U}} = [\hat{\boldsymbol{\mu}}_1 \cdots \hat{\boldsymbol{\mu}}_{l-1}\hat{\boldsymbol{\mu}}_{l+1} \cdots \hat{\boldsymbol{\mu}}_p]$ and $\hat{\boldsymbol{\mu}}_j = P_{\hat{\mathbf{U}}}^{\perp}\boldsymbol{\mu}_j$, for $1 \le j \le p$. If we let $P_{\hat{\mathbf{U}}}^{\perp} = \mathbf{I}$, (12) is further reduced to $\mathbf{w}_l^{\mathrm{LSOSP}} = (\hat{\boldsymbol{\mu}}_l^{\mathrm{T}}\hat{\boldsymbol{\mu}}_l)^{-1}\hat{\boldsymbol{\mu}}_l$, which is exactly the same matched filter used by the LSOSP [3] with the matched signature specified by the desired signature $\hat{\boldsymbol{\mu}}_l$.

C. Relationship Between FVC-FLSMA and LCDA

Recently, a linearly constrained discriminant analysis approach, called LCDA, was developed by Du and Chang [17], where the within-class and between-class scatter matrices were replaced by intradistance and interdistance, respectively, with the class means aligned with mutual orthogonal directions. As shown in [17], the LCDA solution had the same equation specified by (A10). Therefore, the LCDA is essentially the FVC-FLSMA. Furthermore, the total scatter matrix $\mathbf{S}_{\mathrm{T}}$ is the sum of within-class scatter matrix $\mathbf{S}_{\mathrm{W}}$ and between-class scatter matrix $\mathbf{S}_{\mathrm{B}}$ in (3) and is a constant matrix. The problem specified by (6) can be further shown to be equivalent to finding $\mathbf{w}_l$ that satisfies

$$\min_{\mathbf{w}_l}\mathbf{w}_l^{\mathrm{T}}\mathbf{S}_{\mathrm{T}}\mathbf{w}_l \text{ subject to } \mathbf{w}_l^{\mathrm{T}}\boldsymbol{\mu}_j = \delta_{lj}, \quad \text{for } 1 \le j \le p. \tag{13}$$

The solution to (13) can be obtained by $\mathbf{w}_l^* = \mathbf{S}_{\mathrm{T}}^{-1}\mathbf{M}(\mathbf{M}^{\mathrm{T}}\mathbf{S}_{\mathrm{T}}^{-1}\mathbf{M})^{-1}\mathbf{1}_l$, which turns out to be the same as (A10). As shown in [3], the total scatter matrix $\mathbf{S}_{\mathrm{T}}$ was related to the data training sample covariance matrix Σ by $\mathbf{S}_{\mathrm{T}} = N \cdot \Sigma$, where N is total number of training samples. Using this fact, the problem specified by (13) is also equivalent to the following problem

$$\min_{\mathbf{w}_l}\mathbf{w}_l^{\mathrm{T}}\Sigma\mathbf{w}_l \text{ subject to } \mathbf{w}_l^{\mathrm{T}}\boldsymbol{\mu}_j = \delta_{lj}, \qquad \text{for } 1 \le j \le p. \tag{14}$$

The solution to (14) is also $\mathbf{w}_l^* = \Sigma^{-1}\mathbf{M}(\mathbf{M}^{\mathrm{T}}\Sigma^{-1}\mathbf{M})^{-1}\mathbf{1}_l$, which is also the same as (A10).

III. AC-FLSMA

It should be noted that the FVC-FLSMA solution solved by (7) or (A15) is not abundance-constrained in the sense that there is no constraint imposed on the abundance vector α. Therefore, the FVC-FLSMA solution does not guarantee that $\alpha \ge \mathbf{0}$ (that is, $\alpha_j \ge 0$, for all $1 \le j \le p$) and $\sum_{j=1}^{p}\alpha_j = 1$. In order to obtain an AC-FLSMA, we first consider the following least squares problem resulting from the FLSMA with no constraints imposed on the abundance-fraction vector α

$$\min_{\alpha}\left\{(\mathbf{r} - \mathbf{M}\alpha)^{\mathrm{T}}\mathbf{S}_{\mathrm{W}}^{-1}(\mathbf{r} - \mathbf{M}\alpha)\right\}. \tag{15}$$

Since $\mathbf{S}_{\mathrm{W}}$ is positive definite, we express $\mathbf{S}_{\mathrm{W}}^{-1}$ as a square of its square-root form $\mathbf{S}_{\mathrm{W}}^{-1/2}$ by $\mathbf{S}_{\mathrm{W}}^{-1} = \mathbf{S}_{\mathrm{W}}^{-1/2}\mathbf{S}_{\mathrm{W}}^{-1/2}$. Consequently, the $\mathbf{S}_{\mathrm{W}}^{-1}$-weighted LSE in (15) $(\mathbf{r} - \mathbf{M}\alpha)^{\mathrm{T}}\mathbf{S}_{\mathrm{W}}^{-1}(\mathbf{r} - \mathbf{M}\alpha)$ can be simplified as follows:

$$\begin{aligned}
&(\mathbf{r} - \mathbf{M}\alpha)^{\mathrm{T}}\mathbf{S}_{\mathrm{W}}^{-\frac{1}{2}}\mathbf{S}_{\mathrm{W}}^{-\frac{1}{2}}(\mathbf{r} - \mathbf{M}\alpha)\\
&\quad = (\mathbf{r} - \mathbf{M}\alpha)^{\mathrm{T}}\left(\mathbf{S}_{\mathrm{W}}^{-\frac{1}{2}}\right)^{\mathrm{T}}\mathbf{S}_{\mathrm{W}}^{-\frac{1}{2}}(\mathbf{r} - \mathbf{M}\alpha)\\
&\quad = \left(\mathbf{S}_{\mathrm{W}}^{-\frac{1}{2}}\mathbf{r} - \mathbf{S}_{\mathrm{W}}^{-\frac{1}{2}}\mathbf{M}\alpha\right)^{\mathrm{T}}\left(\mathbf{S}_{\mathrm{W}}^{-\frac{1}{2}}\mathbf{r} - \mathbf{S}_{\mathrm{W}}^{-\frac{1}{2}}\mathbf{M}\alpha\right)\\
&\quad = (\tilde{\mathbf{r}} - \tilde{\mathbf{M}}\alpha)^{\mathrm{T}}(\tilde{\mathbf{r}} - \tilde{\mathbf{M}}\alpha)
\end{aligned} \tag{16}$$

which becomes exactly the same least squares mixing problem considered in the LSMA

$$\min_{\alpha}\left\{(\tilde{\mathbf{r}} - \tilde{\mathbf{M}}\alpha)^{\mathrm{T}}(\tilde{\mathbf{r}} - \tilde{\mathbf{M}}\alpha)\right\} \tag{17}$$

with $\tilde{\mathbf{r}} = \mathbf{S}_{\mathrm{W}}^{-1/2}\mathbf{r}$ and $\tilde{\mathbf{M}} = \mathbf{S}_{\mathrm{W}}^{-1/2}\mathbf{M}$. Due to the fact that the process carried out in (16) is similar to the whitening process performed by the covariance matrix in signal detection theory [21], it is referred to as an $\mathbf{S}_{\mathrm{W}}$-whitened process and (17) is called $\mathbf{S}_{\mathrm{W}}$-whitened least squares LSMA.

By virtue of the $\mathbf{S}_{\mathrm{W}}$-whitened least squares LSMA, we can impose two commonly used constraints $\alpha \ge \mathbf{0}$ or $\sum_{j=1}^{p}\alpha_j = 1$ to obtain three types of abundance-constrained least squares FLSMA problems described as follows, which are similar to those discussed in [3], [10], and [13]: abundance sum-to-one constrained least squares (ASCLS), abundance nonnegativity constrained least squares (ANCLS), and FCLS problems:

1) ASCLS-FLSMA problem;

$$\min_{\alpha}\left\{(\tilde{\mathbf{r}} - \tilde{\mathbf{M}}\alpha)^{\mathrm{T}}(\tilde{\mathbf{r}} - \tilde{\mathbf{M}}\alpha)\right\} \text{ subject to } \sum_{j=1}^{p}\alpha_j = 1 \tag{18}$$

2) ANCLS-FLSMA problem;

$$\min_{\alpha}\left\{(\tilde{\mathbf{r}} - \tilde{\mathbf{M}}\alpha)^{\mathrm{T}}(\tilde{\mathbf{r}} - \tilde{\mathbf{M}}\alpha)\right\} \text{ subject to } \alpha \ge \mathbf{0} \tag{19}$$

3) AFCLS-FLSMA problem;

$$\min_{\alpha}\left\{(\tilde{\mathbf{r}} - \tilde{\mathbf{M}}\alpha)^{\mathrm{T}}(\tilde{\mathbf{r}} - \tilde{\mathbf{M}}\alpha)\right\} \text{ subject to } \alpha \ge \mathbf{0} \text{ and } \sum_{j=1}^{p}\alpha_j = 1. \tag{20}$$

The above three abundance-constrained least squares FLSMA problems are precisely the same least squares problems considered in the LSMA [3], [10], [13]. Therefore, (18)–(20) can be solved exactly by the same methods that solve constrained least squares LSMA in [3], [10], and [13].

IV. Experiments

This section conducts two sets of experiments, computer simulations and real-image experiments, to demonstrate the

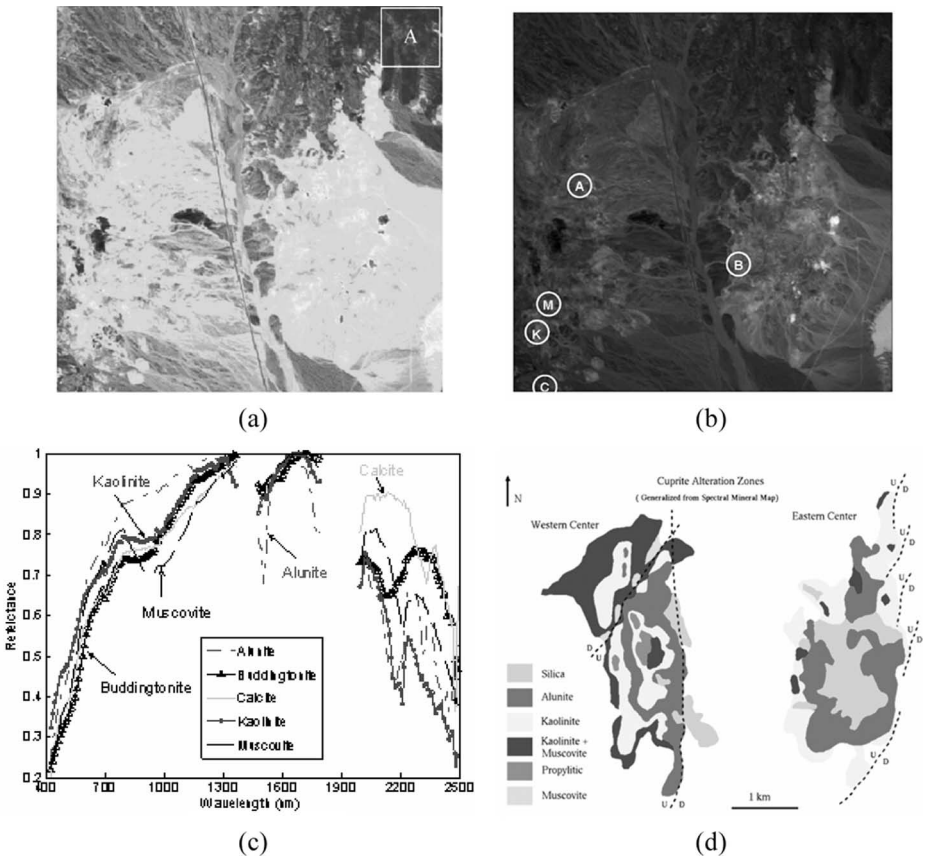

Fig. 1. (a) Spectral band number 170 of the cuprite AVIRIS image scene. (b) Spatial positions of five pure pixels corresponding to minerals: alunite (A), buddingtonite (B), calcite (C), kaolinite (K), and muscovite (M). (c) Five mineral spectra extracted from (b). (d) Alteration map available from USGS [22].

utility of the FLSMA. For abundance-constrained methods, only experiments that implemented the FCLS and AFCLS-FLSMA were included in this section for comparative analysis due to limited space. Nevertheless, according to our conducted experiments, the other two types of the abundance-constrained least squares FLSMA also performed better than their counterparts in least squares LSMA.

The image data set used in experiments is available in reflectance units, after being calibrated and atmospherically corrected by the Airborne Visible/Infrared Imaging Spectrometer (AVIRIS) team at the Jet Propulsion Laboratory. It is the well-known AVIRIS image scene, available online [22] and shown in Fig. 1(a), which was collected over the cuprite mining site, Nevada, in 1997. This 224-band scene is well-understood mineralogically, and has reliable ground truth where the five pure pixels were selected based on the ground truth corresponding to the five different minerals alunite (A), buddingtonite (B), calcite (C), kaolinite (K), and muscovite (M), which are white circled and labeled by A, B, C, K, and M in Fig. 1(b) with their corresponding spectra shown in Fig. 1(c). These pixels were carefully verified using laboratory spectra provided by the U.S. Geological Survey (USGS) (available from http://speclab.cr.usgs.gov). Fig. 1(d) also shows an alteration map for some of the minerals, which was generalized from the ground map provided by the USGS [22] and obtained by Tricorder SW version 3.3. It should be noted that this radiometrically calibrated and atmospherically corrected data set available online from http://aviris.jpl.nasa.gov is provided in reflectance units with 224 spectral channels where the data had been calibrated and atmospherically rectified using the ACORN software package. It was recommendation that bands 1–3, 105–115, and 150–170, due to low water absorption and low SNR in those bands, be removed prior to data processing. As a result, a total number of 189 bands were used for experiments, as shown in Fig. 1(c).

With availability of the ground truth about this image scene, the cuprite image data in Fig. 1 has been widely used for hyperspectral image analysis. In this paper, we also used this image scene as a standard test site to conduct performance evaluation and analysis.

A. *Computer Simulations*

In order to substantiate the FLSMA, we simulated a synthetic image with size of 200 × 200 pixel vectors with 25 panels of various sizes, which are arranged in a 5 × 5 matrix and located at the center of the scene shown in Fig. 2(a). These 25 panels in Fig. 2(a) were implanted in the image background in a way that the background pixels were replaced with the implanted panel pixels where the background was simulated by a single signature $\mathbf{b}$ obtained by averaging pixels in the square area located at upper right corner in Fig. 1(a) marked by A. Finally, this synthetic image with the 25 implanted panels was corrupted by a simulated white Gaussian noise to achieve an SNR of 20 : 1 defined in [6]. The resulting noisy synthetic image is shown in Fig. 2(b). Thus, in this synthetic image scene, there are 100 pure pixels, 20 mixed pixels, and 10 subpixels, all of which were simulated by five distinct pure mineral signatures.

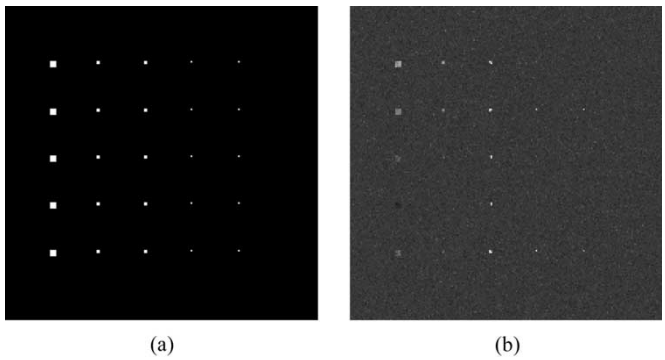

Fig. 2. Synthetic image. (a) Twenty-five simulated panels and (b) synthetic image having the 25 panels simulated in (a) implanted in the background with an additive Gaussian noise to achieve an SNR of 20 : 1.

TABLE I
MIXED PANEL PIXELS IN THE THIRD COLUMN FOR SIMULATIONS

row 1	$p^1_{3,11} = 0.5A + 0.5B$	$p^1_{3,12} = 0.5A + 0.5C$
	$p^1_{3,21} = 0.5A + 0.5K$	$p^1_{3,22} = 0.5A + 0.5M$
row 2	$p^2_{3,11} = 0.5A + 0.5B$	$p^2_{3,12} = 0.5B + 0.5C$
	$p^2_{3,21} = 0.5B + 0.5K$	$p^2_{3,22} = 0.5B + 0.5M$
row 3	$p^3_{3,11} = 0.5A + 0.5C$	$p^3_{3,12} = 0.5B + 0.5C$
	$p^3_{3,21} = 0.5C + 0.5K$	$p^3_{3,22} = 0.5C + 0.5M$
row 4	$p^4_{3,11} = 0.5A + 0.5K$	$p^4_{3,12} = 0.5B + 0.5K$
	$p^4_{3,21} = 0.5C + 0.5K$	$p^4_{3,22} = 0.5K + 0.5M$
row 5	$p^5_{3,11} = 0.5A + 0.5M$	$p^5_{3,12} = 0.5B + 0.5M$
	$p^5_{3,21} = 0.5C + 0.5M$	$p^5_{3,22} = 0.5K + 0.5M$

The five mineral spectral signatures $\{\mathbf{m}_i\}_{i=1}^5$ in Fig. 1(c) were used to simulate these 25 panels, where each row of five panels was simulated by the same mineral signature and each column of five panels has the same size. Among the 25 panels are five 4×4 pure-pixel panels $p^i_{4\times4}$, for $i = 1, \ldots, 5$, lined up in the first column in five separate rows, and five 2×2 pure-pixel panels $p^i_{2\times2}$, for $i = 1, \ldots, 5$, lined up in the second column in five separate rows for pure-pixel classification; the five 2×2 mixed-pixel panels $\{p^i_{3,jk}\}_{j=1,k=1}^{2,2}$, for $i = 1, \ldots, 5$, lined up in the third column in five separate rows for mixed-pixel classification and both the five subpixel panels, $p^i_{4,1}$ for $i = 1, \ldots, 5$ lined up in the fourth column in five separate rows and the five subpixel panels $p^i_{5,1}$, for $i = 1, \ldots, 5$, lined up in the fifth column in five separate rows for subpixel classification. The purpose of introducing the five panels in the third column and subpixel panels in the fourth and fifth columns was designed to conduct a study and analysis on five mineral signatures with different mixing in a pixel and five mineral signatures embedded in single pixels at subpixel scale. Tables I and II tabulate the mixing details of mineral composition in the 20 mixed pixels in the third column in Fig. 2(a) and the five subpixel panels with 50% abundance of mineral signatures in the fourth column and the five subpixel panels with 25% abundance of mineral signatures in the fifth column in Fig. 2(a), respectively.

This synthetic image was particularly designed to evaluate the performance of the FLSMA in addressing three issues, classification of pure pixels in the first and second columns, classification of mixed pixels in the third column, and classification of subpixels with two different abundance fractions in the fourth and fifth columns.

TABLE II
SUBPIXELS IN THE FOURTH AND FIFTH COLUMNS FOR SIMULATIONS

	50% subpixel panels in 4th column	25% subpixel panels in 5th column
row 1	$p^1_{4,1} = 0.5A + 0.5b$	$p^1_{5,1} = 0.25A + 0.75b$
row 2	$p^2_{4,1} = 0.5B + 0.5b$	$p^2_{5,1} = 0.25B + 0.75b$
row 3	$p^3_{4,1} = 0.5C + 0.5b$	$p^3_{5,1} = 0.25C + 0.75b$
row 4	$p^4_{4,1} = 0.5K + 0.5b$	$p^4_{5,1} = 0.25K + 0.75b$
row 5	$p^5_{4,1} = 0.5M + 0.5b$	$p^5_{5,1} = 0.25M + 0.75b$

Fig. 3. Six targets produced by ATGP.

Three scenarios were conducted for performance evaluation: 1) by comparing the FVC-FLSMA to unconstrained classifiers FLDA and LSOSP; 2) by comparing the FVC-FLSMA to signature-constrained classifiers CEM and TCIMF; and 3) by comparing the AFCLS-FLSMA to the fully abundance-constrained classifier FCLS. All the three scenarios were conducted in an unsupervised manner. That is, no prior knowledge about the synthetic image in Fig. 2(b) was assumed. In particular, there was no knowledge about how many signatures would represent the image scene. In this case, we first needed to determine the number of signatures p required to represent the scene. In order to resolve this dilemma, a recently developed concept, called virtual dimensionality (VD) in [3] and [23], was used to estimate this number, which was six.

Example 1 (FVC-FLSMA Versus Unconstrained Classifiers FLDA and LSOSP): In order to produce a set of six desired signatures for the synthetic scene, the automatic target-generation process (ATGP) developed in [24] was used to find six targets $\{\mathbf{e}_j\}_{j=1}^6$, which included five panel pixels specified by all the five different panel signatures $\{\mathbf{p}_i\}_{i=1}^5$ and one background pixel shown in Fig. 3, with the numbers indicating the order that the six target pixels were generated.

The purpose of this example was to demonstrate the performance of the FVC-FLSMA in comparison with the commonly used unconstrained classifiers, the FLDA and LSOSP, where the FLDA is a best known classical pure-pixel classifier and the LSOSP is a widely used least squares LSMA. Since both the FVC-FLSMA and the FLDA required training samples for classification, the Spectral Angle Mapper (SAM) was used as a spectral similarity measure with the threshold set to 0.04 to find pixels that were similar to each of the six target signatures $\{\mathbf{e}_j\}_{j=1}^6$ to form a set of training data for each of the p classes $\{C_j\}_{j=1}^6$. The value of threshold 0.04 was set

empirically according to our experiments and experience. Then, the means of each of the six classes were further calculated $\{\boldsymbol{\mu}_j\}_{j=1}^{6}$ to form the desired signature matrix $\mathbf{M}$ for the FVC-FLSMA and the FLDA. However, for the LSOSP, the target signature matrix was formed directly by the ATGP-generated target pixels $\{\mathbf{e}_j\}_{j=1}^{6}$ because LSOSP did not need training samples. Fig. 4(a)–(c) shows the classification results of the 25 panels in Fig. 2(b) produced by the FVC-FLSMA, FLDA, and LSOSP, respectively. Since both the FVC-FLSMA and the LSOSP are mixed-pixel classifiers, they produced grayscale fractional-abundance images for each of five panel classes in Fig. 4(a) and (c), respectively. To the contrary, the FLDA is a pure-pixel-based class-labeling classifier. Thus, the images shown in Fig. 4(b) are five classification maps, one for each of panel classes.

As shown in Fig. 4(a)–(c), the FLDA was the worst among the three classifiers in the sense that it misclassified $p_{4,1}^{1}$, $p_{4,1}^{5}$ as the second panel signature, and also $p_{4,1}^{2}$, $p_{4,1}^{4}$, $p_{5,1}^{1}$, $p_{5,1}^{2}$, $p_{5,1}^{4}$, $p_{5,1}^{5}$ as the third panel signature. Comparing Fig. 4(a)–(c), we also see that the FVC-FLSMA performed better than the LSOSP in terms of background suppression for panels in the third row and reduction of the false alarms caused by other panels. This experiment demonstrated that the FVC-FLSMA performed the best among the three classifiers in terms of target detection and classification as well as background suppression and small false-alarm rate.

Example 2 (FVC-FLSMA Versus Target Signature-Constrained Classifiers CEM and TCIMF): This example was designed to compare the FVC-FLSMA against two target signature-constrained classifiers CEM and TCIMF [3], [19]. The FVC-FLSMA implemented in this example was the same one in Example 1. The CEM was implemented by considering one of the five ATGP-generated panel signatures $\mathbf{e}_1 = \mathbf{p}_5$, $\mathbf{e}_2 = \mathbf{p}_1$, $\mathbf{e}_4 = \mathbf{p}_4$, $\mathbf{e}_5 = \mathbf{p}_2$, $\mathbf{e}_6 = \mathbf{p}_3$ in Example 1 as a desired target signature $\mathbf{d}$ separately, and was performed for each of five minerals. The TCIMF was implemented in a similar manner that the CEM was implemented but it also used the other five ATGP-generated target pixels for undesired target annihilation. Fig. 5(a)–(b) shows the classification results of the CEM and TCIMF, respectively, where the TCIMF performed slightly better than the CEM did due to the fact that the CEM produced more false alarms for panels in the third, fourth, and fifth rows.

Now, comparing Fig. 5(b) to Fig. 4(a), both the FVC-FLSMA and the TCIMF performed comparably, but the FVC-FLSMA performed slightly better in terms of background suppression in panels in the third row.

Example 3 (AFCLS-FLSMA Versus Fully Abundance-Constrained Classifier FCLS): This example studies the relative performance of the AFCLS-FLSMA to the FCLS classifier in [3] and [13], where the required target knowledge used for both the AFCLS-FLSMA and FCLS was obtained in Example 1. Since the abundance fractions are of major interest, only fully abundance-constrained classifiers were considered. Fig. 6 graphically plots the abundance fractions of the panel pixels obtained by the AFCLS-FLSMA and FCLS for abundance quantification analysis, respectively, where it clearly shows that the AFCLS-LSMA performed significantly better than the FCLS according to the accuracy of estimated abundance fractions plotted in Fig. 6 for all 130 pure and mixed panel pixels plus subpixel panels. Additionally, the LSEs calculated for the AFCLS-FLSMA and FCLS were 0.176 and 0.884, respectively, which further demonstrated that the AFCLS-FLSMA outperformed the FCLS.

B. Real-Image Experiments

In this section, the AVIRIS cuprite image scene in Fig. 1(a) was used for experiments. One major difference between the real cuprite image scene and the simulated synthetic image in Fig. 2(b) used for computer simulations is that the image background in Fig. 1 was unknown compared to the image background in Fig. 2(b), which was simulated by complete knowledge.

Since no prior knowledge about the cuprite scene is available, two preprocessing steps are needed prior to implementation of the FLSMA. One is to determine the number of classes in the image data. If we translate that each class is represented by one spectrally distinct signature, the number of classes can be determined by the number of spectrally distinct signatures present in the data, which can be estimated by VD. Table III lists the values of the VD with various false-alarm probabilities P_{F}.

For our experiments, the VD was chosen to be 22, with the false-alarm probability $P_{\mathrm{F}} = 10^{-4}$. To find these 22 distinct signatures, ATGP was also implemented for this purpose. Fig. 7 shows the found 22 target pixels $\{\mathbf{t}_k\}_{k=1}^{22}$ with numbers indicating the orders that target pixels were found. Since each of the 22 target pixels represents one single distinct class, a second preprocessing is to find training samples for each of the 22 target classes, denoted by $\{C_i\}_{i=1}^{22}$. It has been shown in [3] that the CEM is very effective in target detection. Therefore, the CEM was used for our experiments to find training samples $\{C_i\}_{i=1}^{22}$, where the threshold selected for the CEM was empirically set to 0.4. Table IV provides the numbers of training samples found for each of 22 classes $\{C_i\}_{i=1}^{22}$, where the numbers in the top row indicate class numbers and the numbers in the bottom row are the number of training samples found by the CEM for each of the 22 classes.

In order to find which ATGP-generated target pixels are specified by five minerals, a spectral measure is required for identification. According to recent results reported in [25], the RMFD defined by

$$\mathrm{RMFD}(\mathbf{t}_i, \mathbf{t}_j) = \mathbf{t}_i^{\mathrm{T}} \mathbf{R}^{-1} \mathbf{t}_j \tag{21}$$

was shown to perform significantly better and more effectively than did the commonly used pixel level-based SAM in discrimination and identification of subpixels and mixed pixels for real hyperspectral images, where the matrix $\mathbf{R}$ is the sample correlation matrix and $\mathbf{t}_i$ and $\mathbf{t}_j$ are two target pixels to be discriminated. Therefore, the RMFD was used to identify the 22 ATGP-generated target pixels against the five minerals of interest A, B, C, K, and M by the RMFD via (21), where the signatures of the five minerals in Fig. 1(c) were used. Table V is the identification results of these 22 ATGP-generated target pixels, where $\mathbf{t}_{11}$, $\mathbf{t}_5$, $\mathbf{t}_{10}$, $\mathbf{t}_4$, and $\mathbf{t}_8$ were identified and highlighted by shade as the five minerals A, B, C, K, and M, respectively. For the methods that involve training samples such

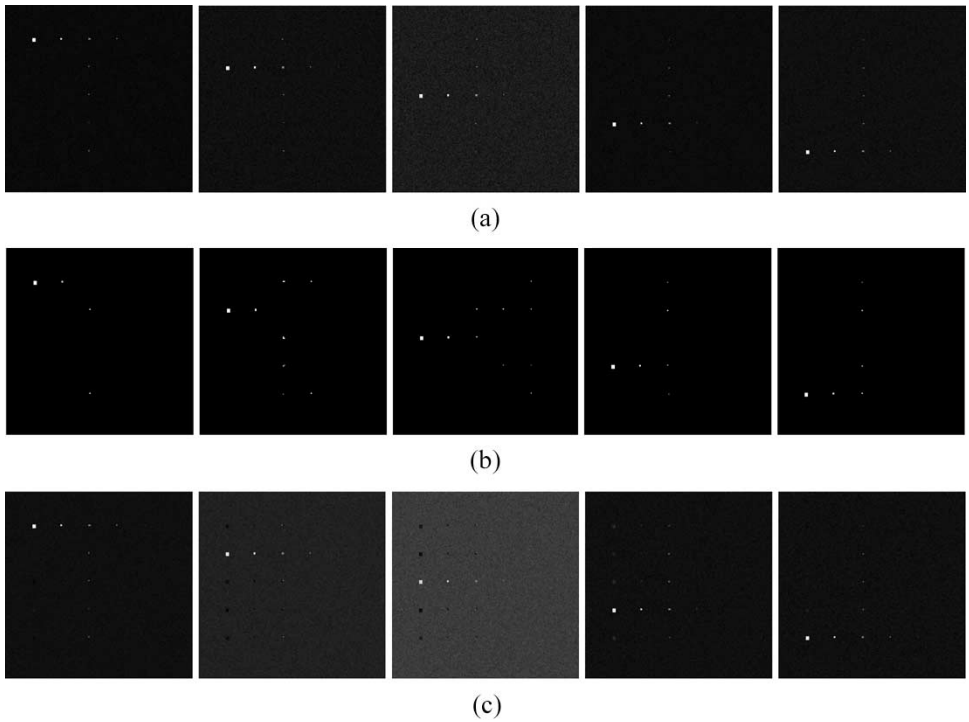

Fig. 4. Classification results of the 25 panels in Fig. 2(b) produced by the FVC-FLSMA, FLDA, and LSOSP, respectively. (a) FVC-FLSMA, (b) FLDA, and (c) LSOSP.

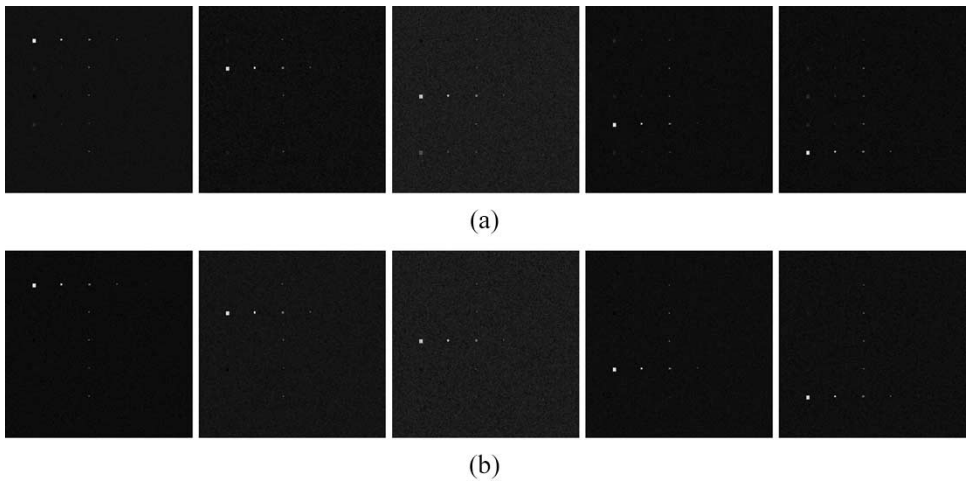

Fig. 5. Classification results of the 25 panels in Fig. 2(b) produced by the CEM and TCIMF, respectively. (a) CEM and (b) TCIMF.

as FVC-FLSMA, FLDA, and AFCLS-FLSMA, the CEM-found training samples in $\{C_i\}_{i=1}^{22}$ through the 22 ATGP-generated target pixels $\{\mathbf{t}_k\}_{k=1}^{22}$ were used to form the desired training pool. For the LSOSP and FCLS, the means $\boldsymbol{\mu}_{11}$, $\boldsymbol{\mu}_5$, $\boldsymbol{\mu}_{10}$, $\boldsymbol{\mu}_4$, and $\boldsymbol{\mu}_8$ of the training classes specified by the five pixels $\mathbf{t}_{11}$, $\mathbf{t}_5$, $\mathbf{t}_{10}$, $\mathbf{t}_4$, and $\mathbf{t}_8$ were calculated to form the signature matrix, while the CEM and TCIMF used the five pixels $\mathbf{t}_{11}$, $\mathbf{t}_5$, $\mathbf{t}_{10}$, $\mathbf{t}_4$, and $\mathbf{t}_8$ as the target pixels.

Fig. 8 also shows the results of the FVC-FLSMA, FLDA, LSOSP, CEM, and TCIMF, respectively. According to the ground truth provided in Fig. 1(b) and (d), the FVC-FLSMA seemed to perform the best in terms of classifying the four minerals alunite (A), calcite (C), kaolinite (K), and muscovite (M), except buddingtonite (B) in Fig. 8(a), while the LSOSP was the worst. Surprisingly, the FLDA also performed reasonable well in the classification of all five minerals. The reason that the FVC-LSMA performed poorly on the classification of buddingtonite might be due to the fact that the training samples were heavily mixed and could not characterize the buddingtonite. However, such dilemma could be resolved by imposing abundance constraints on the found training samples, as shown in Fig. 9, where both the AFCLS-FLSMA and FCLS significantly improved their unconstrained counterparts. In particular, the AFCLS-FLSMA clearly outperformed the FCLS.

Most interestingly, if we compare the classification result of buddingtonite in Fig. 8 to that in Fig. 9, the FVC-FLSMA performed very poorly in Fig. 8(a), but its counterpart, the AFCLS-FLSMA, turned out to be the best in Fig. 9(a) among all the unconstrained or abundance-constrained classifiers if abundance constraints were fully imposed on training samples. As a comment made previously on simulation results, the LSOSP and FCLS might perform well if the target signatures

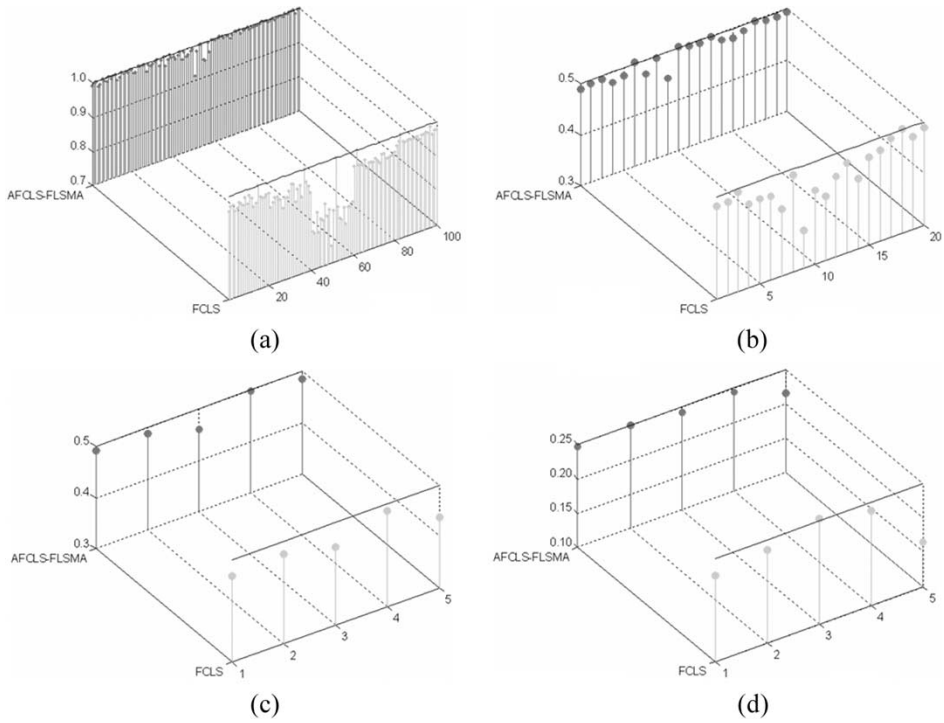

Fig. 6. Graphical representation of abundance fractions of 130 panel pixels in Fig. 2(b) for visual assessment. (a) One hundred pure-pixel panels in the first and second columns. (b) Twenty mixed pixels in the third column. (c) Fifty percent subpixel panels in the fourth column. (d) Twenty-five percent subpixel panels in fifth column.

TABLE III
VD ESTIMATED FOR THE CUPRITE SCENE WITH VARIOUS FALSE-ALARM PROBABILITIES

	$P_F = 10^{-1}$	$P_F = 10^{-2}$	$P_F = 10^{-3}$	$P_F = 10^{-4}$	$P_F = 10^{-5}$
VD	34	30	24	22	20

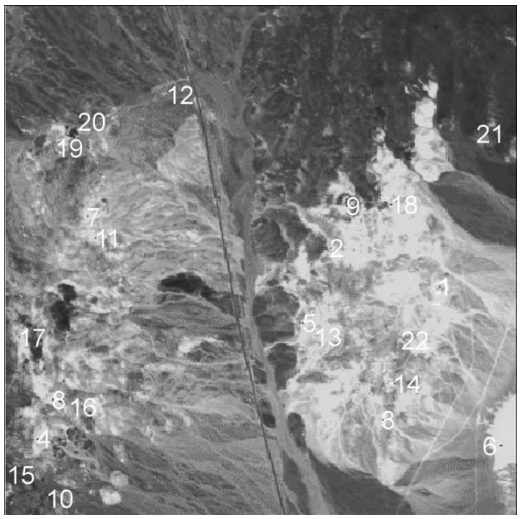

Fig. 7. ATGP-generated 22 target pixels.

were more accurate. In this case, if we used the five ATGP-generated target pixels $\mathbf{t}_{11}$, $\mathbf{t}_5$, $\mathbf{t}_{10}$, $\mathbf{t}_4$, and $\mathbf{t}_8$ to replace the means of the five training classes as the signature matrix, the classification results in Fig. 10(a) and (b) show that the LSOSP performance was significantly improved in Fig. 10(a), while the FCLS performance remained about the same in Fig. 10(b). This experiment demonstrated that fully abundance-constrained classifiers were generally preferred in mixed-pixel classification and subpixel detection.

According to the experiments conducted in this paper, two concluding remarks are noteworthy.

1) The main strength of the FVC-LSMA is its ability in pattern classification, not in target abundance fractions. In order to resolve this dilemma, an AC-FLSMA approach can be further developed to accurately estimate the abundance fractions of mixed pixels and subpixels. As shown in the experiments, when such abundance constraints are imposed on the FLSMA, the resulting performance was significantly improved and better than the fully constrained spectral unmixing method FCLS.
2) In order to provide consistent experimental results, only one real hyperspectral image, the cuprite image scene, was used throughout the paper. As a matter of fact, many simulation results and real-image experiments have been conducted and were not included in this paper to further substantiate our proposed FLSMA due to limited space. In particular, similar experiments based on HYperspectral Digital Imagery Collection Experiment (HYDICE) data were also conducted with similar conclusions in [27].

V. CONCLUSION

This paper presents a new approach to LSMA, referred to as FLSMA, which directly extends the well-known FLDA to the LSMA in two different ways. One is called feature-vector-constrained FLSMA (FVC-FLSMA), which constrains the Fisher's ratio-generated feature vectors to mutual orthogonal directions. Another is called AC-FLSMA, which imposes the sum-to-one and nonnegativity constraints on abundance fractions in the least squares sense. It has been shown that the FVC-FLSMA operates the same functional form as the LCMV

TABLE IV
NUMBER OF TRAINING SAMPLES GENERATED BY CEM FOR EACH CLASS WITH A TOTAL NUMBER OF 710 PIXELS

1	2	3	4	5	6	7	8	9	10	11	12	13	14	15	16	17	18	19	20	21	22
53	8	24	45	80	56	14	50	42	75	5	2	120	7	32	7	55	9	13	3	2	8

TABLE V
RMFD-BASED SPECTRAL SIMILARITY VALUES OBTAINED BY COMPARING THE 22 ATGP-GENERATED TARGET PIXELS $\{\mathbf{t}_k\}_{k=1}^{22}$ AGAINST THE FIVE MINERAL REFLECTANCE SIGNATURES IN FIG. 1(c)

	alunite	buddingtonite	calcite	kaolinite	muscovite
$\mathbf{t}_1$	-75.797	31.317	-28.665	219.495	-11.012
$\mathbf{t}_2$	0.805	-19.298	1.985	-44.371	5.26
$\mathbf{t}_3$	-27.24	18.331	-45.162	-11.048	48.391
$\mathbf{t}_4$	64.2	32.256	3.636	501.274	-34.598
$\mathbf{t}_5$	-52.123	653.806	-29.931	84.771	13.606
$\mathbf{t}_6$	-30.621	-16.319	-9.205	-55.37	-0.611
$\mathbf{t}_7$	18.964	5.726	-1.894	-93.397	-89.431
$\mathbf{t}_8$	16.599	24.899	-48.725	-18.549	659.342
$\mathbf{t}_9$	-23.328	49.014	-11.676	28.262	5.727
$\mathbf{t}_{10}$	-36.717	-19.661	155.107	-32.625	-28.057
$\mathbf{t}_{11}$	175.024	8.683	6.163	-49.031	-12.907
$\mathbf{t}_{12}$	106.105	-268.802	45.073	-157.747	-287.89
$\mathbf{t}_{13}$	-22.663	380.048	-29.727	116.165	7.55
$\mathbf{t}_{14}$	-15.91	-20.239	31.349	-48.553	55.892
$\mathbf{t}_{15}$	-35.627	16.746	4.753	-55.738	-11.419
$\mathbf{t}_{16}$	-14.424	-6	44.142	-73.375	62.841
$\mathbf{t}_{17}$	-13.663	-14.832	-0.51	-4.559	-67.923
$\mathbf{t}_{18}$	-12.49	-34.573	-1.947	-5.194	362.067
$\mathbf{t}_{19}$	-30.695	58.146	-16.503	25.474	-43.365
$\mathbf{t}_{20}$	15.013	-113.88	40.041	-44.066	281.805
$\mathbf{t}_{21}$	30.724	-6.595	-3.963	13.053	-1.558
$\mathbf{t}_{22}$	27.038	-6.407	4.822	21.159	18.228

classifier does, with the only difference that the data correlation matrix used in the LCMV is replaced by the within-class scatter matrix in the FLSMA. Because the within-class scatter matrix is a more effective measure than the data correlation matrix in pattern classification, the FVC-FLSMA generally performs better than the LCMV in mixed-pixel classification provided that an appropriate set of training sample data is used. Additionally, the LCDA can be also shown to be the same as the FVC-FLSMA. As for the AC-FLSMA, there are also three types of constraints that can be imposed in parallel in the same fashion that three types of constraints are imposed on the LSMA. The resulting AC-LSMA is called ASCLS-FLSMA, ANCLS-FLSMA, and AFCLS-FLSMA, with their respective counterparts in the abundance-constrained least squares LSMA, SCLS, NCLS, and FCLS. Since the mixed-pixel classification is performed by the proposed AC-FLSMA using Fisher's ratio as a classification measure and LSE as an abundance estimation criterion, the AC-FLSMA also performs better than the abundance-constrained least squares LSMA and abundance-unconstrained FVC-FLSMA given that the training data are appropriately selected. As shown in our experiments conducted in this paper as well as the experiments in [27], the unsupervised FLSMA can perform as well as the FLSMA can if the training data generated unsupervisedly provide sufficient representative samples for each of classes. Furthermore, the performance of the FLSMA relies heavily on the training samples. If the image is ill represented by a given sample pool, the FLSMA may perform poorly.

APPENDIX

In this appendix, we derive the FVC-LSMA solution to the problem specified by (6). In analogy with the same argument developed in [17], the numerator $\mathbf{w}_l^{\mathrm{T}}\mathbf{S}_{\mathrm{B}}\mathbf{w}_l$ can be further simplified by

$$\begin{aligned}\mathbf{w}_l^{\mathrm{T}}\mathbf{S}_{\mathrm{B}}\mathbf{w}_l &= \mathbf{w}_l^{\mathrm{T}}\left[\sum_{j=1}^{p} n_j(\boldsymbol{\mu}_j-\boldsymbol{\mu})(\boldsymbol{\mu}_j-\boldsymbol{\mu})^{\mathrm{T}}\right]\mathbf{w}_l \\ &= n_l - 2\sum_{j=1}^{p} n_j\delta_{lj}\mathbf{w}_l^{\mathrm{T}}\boldsymbol{\mu} + \sum_{j=1}^{p} n_j\left(\mathbf{w}_l^{T}\boldsymbol{\mu}\right)\left(\mathbf{w}_l^{\mathrm{T}}\boldsymbol{\mu}\right)^{\mathrm{T}}\end{aligned} \tag{A1}$$

with $\boldsymbol{\mu}$ being the global mean of the sample training data. Since

$$2\sum_{j=1}^{p} n_l\delta_{lj}\mathbf{w}_l^{\mathrm{T}}\boldsymbol{\mu} = 2\sum_{j=1}^{p} n_l\delta_{lj}\left[\mathbf{w}_l^{\mathrm{T}}\left(\frac{1}{n\sum_{k=1}^{p} n_k\boldsymbol{\mu}_k}\right)\right] = \frac{2n_l^2}{n} \tag{A2}$$

and

$$\sum_{j=1}^{p} n_j\left(\mathbf{w}_l^{\mathrm{T}}\boldsymbol{\mu}\right)\left(\mathbf{w}_l^{T}\boldsymbol{\mu}\right)^{\mathrm{T}} = \sum_{j=1}^{p} n_j\left(\frac{n_l}{n}\right)^2 = \frac{n_l^2}{n} \tag{A3}$$

the $\mathbf{w}_l^{\mathrm{T}}\mathbf{S}_{\mathrm{B}}\mathbf{w}_l$ in (A1) can be further reduced to

$$\mathbf{w}_l^{\mathrm{T}}\mathbf{S}_{\mathrm{B}}\mathbf{w}_l = n_l - 2\left(\frac{n_l^2}{n}\right) + \left(\frac{n_l^2}{n}\right) = n_l - \left(\frac{n_l^2}{n}\right) \tag{A4}$$

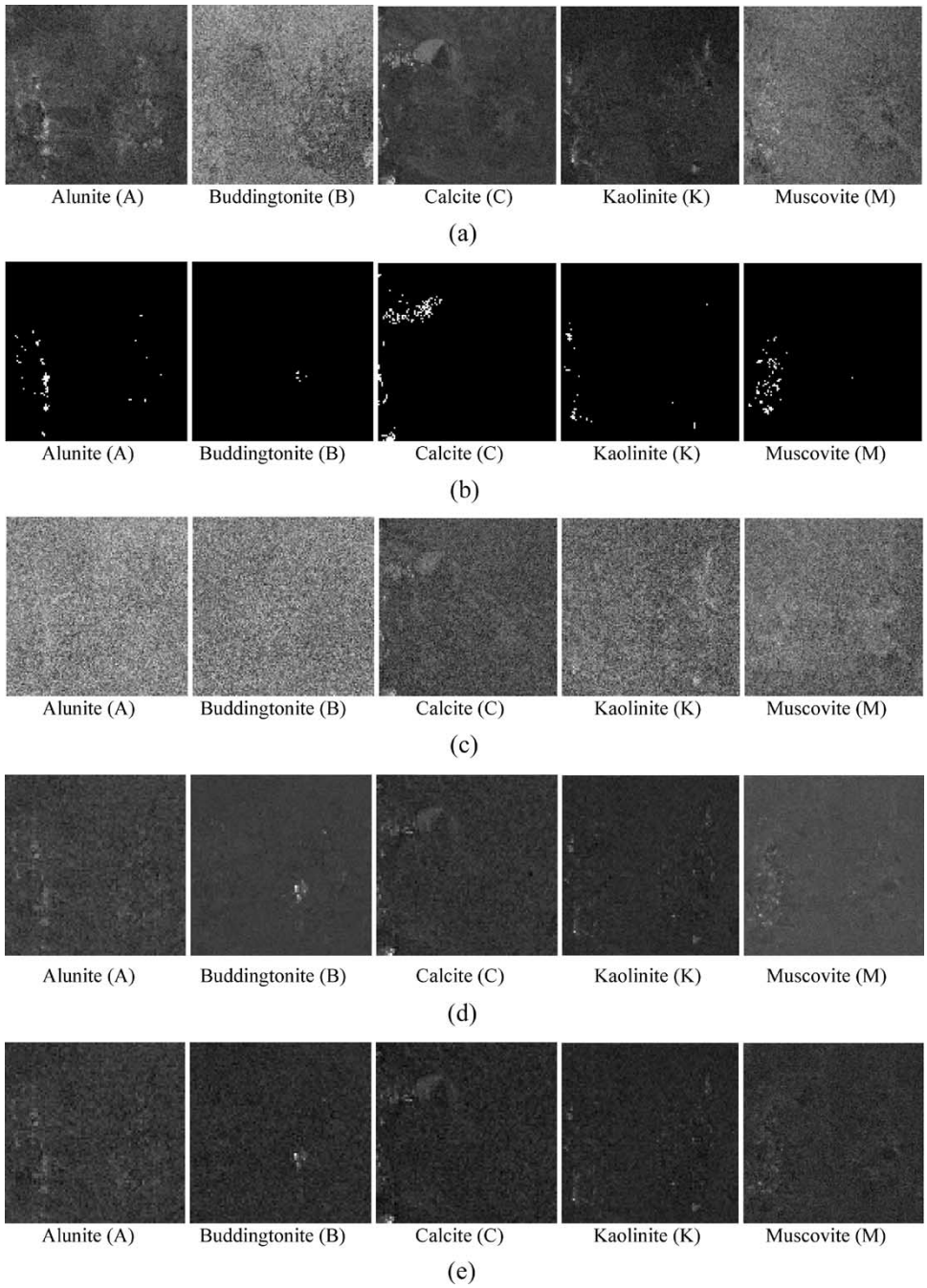

Fig. 8. Classification results of the five minerals by FVC-FLSMA, FLDA, LSOSP, CEM, and TCIMF, respectively. (a) FVC-FLSMA, (b) FLDA, (c) LSOSP, (d) CEM, and (e) TCIMF.

which is independent of $\mathbf{w}_l$. As a consequence, the FVC-FLSMA problem specified by (6) is reduced to the one finding $\mathbf{w}_l^{\mathrm{FVC-FLSMA}}$, which satisfies the following constrained optimization problem:

$$\min_{\mathbf{w}_l} \mathbf{w}_l^{\mathrm{T}} \mathbf{S}_{\mathrm{W}} \mathbf{w}_l \text{ subject to } \mathbf{w}_l^{\mathrm{T}} \boldsymbol{\mu}_j = \delta_{lj}, \qquad \text{for } 1 \le j \le p. \quad \text{(A5)}$$

In order to solve the above problem, we define an objection function for each $\mathbf{w}_l$ given by

$$J(\mathbf{w}_l) = \mathbf{w}_l^{\mathrm{T}} \mathbf{S}_{\mathrm{W}} \mathbf{w}_l + \sum_{j=1}^{p} \lambda_j^l \left(\mathbf{w}_l^{\mathrm{T}} \boldsymbol{\mu}_j - \delta_{lj} \right) \quad \text{(A6)}$$

where $\{\lambda_j^l\}_{j=1,l=1}^{p,p}$ are Lagrange multipliers. Differentiating (A6) with respect to $\mathbf{w}_l$ yields

$$\left. \frac{\partial J(\mathbf{w}_l)}{\partial \mathbf{w}_l} \right|_{\mathbf{w}_l^{\mathrm{FVC-FLSMA}}} = 2\mathbf{S}_{\mathrm{W}} \mathbf{w}_l^{\mathrm{FLSMA}} + \sum_{j=1}^{p} \lambda_j^l \boldsymbol{\mu}_j = 0 \quad \text{(A7)}$$

which results in

$$\begin{aligned} &2\mathbf{S}_{\mathrm{W}} \mathbf{w}_l^{\mathrm{FVC-FLSMA}} + \sum_{j=1}^{p} \lambda_j^l \boldsymbol{\mu}_j \\ &\quad = 2\mathbf{S}_{\mathrm{W}} \mathbf{w}_l^{\mathrm{FVC-FLSMA}} + \mathbf{M}\lambda^l = 0 \\ &\quad \Rightarrow \mathbf{w}_l^{\mathrm{FVC-FLSMA}} = -\left(\frac{1}{2}\right) \mathbf{S}_{\mathrm{W}}^{-1} \mathbf{M} \lambda^l \end{aligned} \quad \text{(A8)}$$

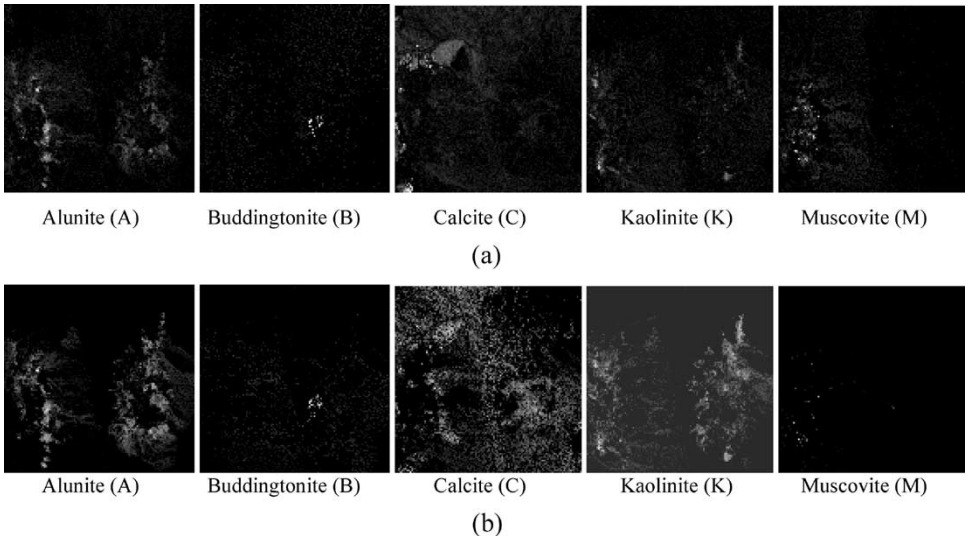

Fig. 9. Classification results of the five minerals produced by AFCLS-FLSMA and FCLS, respectively. (a) AFCLS-FLSMA and (b) FCLS.

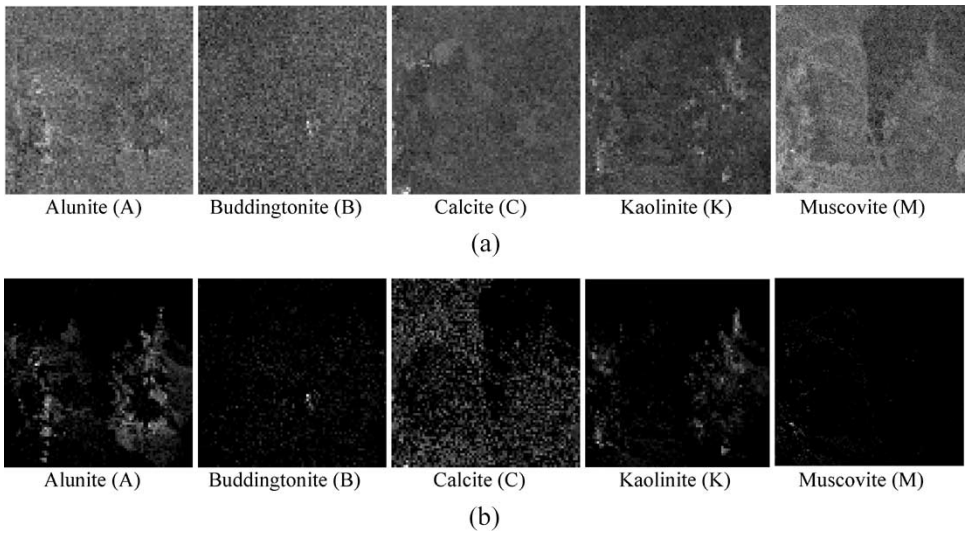

Fig. 10. Classification results produced by LSOSP and FCLS using the five ATGP-generated target pixels $\mathbf{t}_{11}$, $\mathbf{t}_5$, $\mathbf{t}_{10}$, $\mathbf{t}_4$, and $\mathbf{t}_8$ as the target information. (a) LSOSP and (b) FCLS.

where $\mathbf{M} = \lfloor \boldsymbol{\mu}_1 \ \boldsymbol{\mu}_2 \ \cdots \ \boldsymbol{\mu}_p \rfloor$ and $\boldsymbol{\lambda}^l = (\lambda_1^l, \lambda_2^l, \ldots, \lambda_p^l)^{\mathrm{T}}$ is the Largrange multiplier vector.

Using the constraint that $(\mathbf{w}_l^{\mathrm{FVC-FLSMA}})^{\mathrm{T}} \boldsymbol{\mu}_j = \delta_{lj}$ for $1 \leq j \leq p$, the Lagrange multiplier vector λ^l can be obtained by

$$\lambda^l = -2\left(\mathbf{M}^{\mathrm{T}}\mathbf{S}_{\mathrm{W}}^{-1}\mathbf{M}\right)^{-1}\mathbf{1}_l \text{ with } \mathbf{1}_l = (0,\ldots,0,\underbrace{1}_{l},0,\ldots,0)^{\mathrm{T}}. \tag{A9}$$

Substituting (A9) for λ^l in (A8) yields the lth weight vector $\mathbf{w}_l^{\mathrm{FVC-FLSMA}}$ given by

$$\mathbf{w}_l^{\mathrm{FVC-FLSMA}} = \mathbf{S}_{\mathrm{W}}^{-1}\mathbf{M}\left(\mathbf{M}^{\mathrm{T}}\mathbf{S}_{\mathrm{W}}^{-1}\mathbf{M}\right)^{-1}\mathbf{1}_l. \tag{A10}$$

Furthermore, we can even derive a matrix form for all the optimal solutions $\{\mathbf{w}_l^{\mathrm{FVC-FLSMA}}\}_{l=1}^{p}$ for (A5). If $\mathbf{W}^{\mathrm{FVC-FLSMA}} = \lfloor \mathbf{w}_1^{\mathrm{FVC-FLSMA}} \ \mathbf{w}_2^{\mathrm{FVC-FLSMA}} \ \cdots \ \mathbf{w}_p^{\mathrm{FVC-FLSMA}} \rfloor$ and $\Gamma = \lfloor \lambda^1 \lambda^2 \cdots \lambda^p \rfloor$, the constraints in (A5) can be expressed in the following matrix form:

$$(\mathbf{W}^{\mathrm{FVC-FLSMA}})^{\mathrm{T}}\mathbf{M} = \mathbf{I} \tag{A11}$$

and (A8) becomes

$$\mathbf{W}^{\mathrm{FVC-FLSMA}} = -\left(\frac{1}{2}\right)\mathbf{S}_{\mathrm{W}}^{-1}\mathbf{M}\Gamma. \tag{A12}$$

Using (A12) and the constraint specified by (A11) we obtain

$$-\left(\frac{1}{2}\right)\Gamma^{\mathrm{T}}\mathbf{M}^{\mathrm{T}}\mathbf{S}_{\mathrm{W}}^{-1}\mathbf{M} = \mathbf{I} \Rightarrow \Gamma^{\mathrm{T}} = -2\left(\mathbf{M}^{\mathrm{T}}\mathbf{S}_{\mathrm{W}}^{-1}\mathbf{M}\right)^{-1}. \tag{A13}$$

Substituting (A13) into (A12) results in the FVC-FLSMA solution in a matrix form given by

$$\begin{aligned}\mathbf{W}^{\mathrm{FVC-FLSMA}} &= \mathbf{S}_{\mathrm{W}}^{-1}\mathbf{M}\left(\mathbf{M}^{\mathrm{T}}\mathbf{S}_{\mathrm{W}}^{-1}\mathbf{M}\right)^{-\mathrm{T}} \\ &= \mathbf{S}_{\mathrm{W}}^{-1}\mathbf{M}\left(\mathbf{M}^{\mathrm{T}}\mathbf{S}_{\mathrm{W}}^{-1}\mathbf{M}\right)^{-1}.\end{aligned} \tag{A14}$$

where $\mathbf{X}^{-\mathrm{T}}$ is defined by $\mathbf{X}^{-\mathrm{T}} \equiv (\mathbf{X}^{-1})^{\mathrm{T}}$. Applying the $\mathbf{W}^{\mathrm{FVC-FLSMA}}$ to a sample vector $\mathbf{r}$, the abundance vector $\alpha(\mathbf{r})$ associated with $\mathbf{r}$ can be expressed as

$$\alpha(\mathbf{r}) = (\mathbf{W}^{\mathrm{FVC-FLSMA}})^{\mathrm{T}}\mathbf{r} = \left(\mathbf{M}^{\mathrm{T}}\mathbf{S}_{\mathrm{W}}^{-1}\mathbf{M}\right)^{-1}\mathbf{M}^{\mathrm{T}}\mathbf{S}_{\mathrm{W}}^{-1}\mathbf{r}. \quad \text{(A15)}$$

ACKNOWLEDGMENT

The authors would like to thank A. Plaza who provided the cuprite image scene along with its ground truth used in this paper. In particular, the authors would like to acknowledge his valuable suggestions and useful discussions with the scene.

REFERENCES

[1] J. B. Adams and M. O. Smith, "Spectral mixture modeling: A new analysis of rock and soil types at the Viking Lander 1 suite," *J. Geophys. Res.*, vol. 91, no. B8, pp. 8098–8112, Jul. 10, 1986.

[2] J. B. Adams, M. O. Smith, and A. R. Gillespie, "Image spectroscopy: Interpretation based on spectral mixture analysis," in *Remote Geochemical Analysis: Elemental and Mineralogical Composition*, C. M. Pieters and P. A. Englert, Eds. Cambridge, U.K.: Cambridge Univ. Press, 1993, pp. 145–166.

[3] C.-I Chang, *Hyperspectral Imaging: Techniques for Spectral Detection and Classification*. New York: Plenum, 2003.

[4] D. E. Sabol, J. B. Adams, and M. O. Smith, "Quantitative sub-pixel spectral detection of targets in multispectral images," *J. Geophys. Res.*, vol. 97, no. E2, pp. 2659–2672, Feb. 1992.

[5] M. O. Smith, J. B. Adams, and D. E. Sabol, "Spectral mixture analysis-new strategies for the analysis of multispectral data," in *Image Spectroscopy—A Tool for Environmental Observations*, J. Hill and J. Mergier, Eds. Dordrecht, The Netherlands: Kluwer, 1994, pp. 125–143.

[6] J. C. Harsanyi and C.-I Chang, "Hyperspectral image classification and dimensionality reduction: An orthogonal subspace projection approach," *IEEE Trans. Geosci. Remote Sens.*, vol. 32, no. 4, pp. 779–785, Jul. 1994.

[7] J. J. Settle, "On the relationship between spectral unmixing and subspace projection," *IEEE Trans. Geosci. Remote Sens.*, vol. 34, no. 4, pp. 1045–1046, Jul. 1996.

[8] C.-I Chang, "Further results on relationship between spectral unmixing and subspace projection," *IEEE Trans. Geosci. Remote Sens.*, vol. 36, no. 3, pp. 1030–1032, May 1998.

[9] C.-I Chang, X. Zhao, M. L. G. Althouse, and J.-J. Pan, "Least squares subspace projection approach to mixed pixel classification in hyperspectral images," *IEEE Trans. Geosci. Remote Sens.*, vol. 36, no. 3, pp. 898–912, May 1998.

[10] J. J. Settle and N. A. Drake, "Linear mixing and estimation of ground cover proportions," *Int. J. Remote Sens.*, vol. 14, no. 6, pp. 1159–1177, 1993.

[11] Y. E. Shimabukuro and J. A. Smith, "The least-squares mixing models to generate fraction images derived from remote sensing multispectral data," *IEEE Trans. Geosci. Remote Sens.*, vol. 29, no. 1, pp. 16–20, Jan. 1991.

[12] S. Tompkins, J. F. Mustarrd, C. M. Pieters, and D. W. Forsyth, "Optimization of targets for spectral mixture analysis," *Remote Sens. Environ.*, vol. 59, no. 3, pp. 472–489, 1997.

[13] D. Heinz and C.-I Chang, "Fully constrained least squares linear mixture analysis for material quantification in hyperspectral imagery," *IEEE Trans. Geosci. Remote Sens.*, vol. 39, no. 3, pp. 529–545, Mar. 2001.

[14] B. H. Juang and S. Katagiri, "Discriminative learning for minimum classification errors," *IEEE Trans. Signal Process.*, vol. 40, no. 12, pp. 3043–3054, Dec. 1992.

[15] R. O. Duda and P. E. Hart, *Pattern Classification and Scene Analysis*. New York: Wiley, 1973.

[16] H. Soltanian-Zadeh, J. P. Windham, and D. J. Peck, "Optimal linear transformation for MRI feature extraction," *IEEE Trans. Med. Imag.*, vol. 15, no. 6, pp. 749–767, Dec. 1996.

[17] Q. Du and C.-I Chang, "A linear constrained distance-based discriminant analysis for hyperspectral image classification," *Pattern Recognit.*, vol. 34, no. 2, pp. 361–373, Feb. 2001.

[18] C.-I Chang, "Target signature-constrained mixed pixel classification for hyperspectral imagery," *IEEE Trans. Geosci. Remote Sens.*, vol. 40, no. 5, pp. 1065–1081, May 2002.

[19] H. Ren and C.-I Chang, "Target-constrained interference-minimized approach to subpixel target detection for hyperspectral imagery," *Opt. Eng.*, vol. 39, no. 12, pp. 3138–3145, Dec. 2000.

[20] J. C. Harsanyi, *Detection and Classification of Subpixel Spectral Signatures in Hyperspectral Image Sequences*. Baltimore County: Dept. Elect. Eng., Univ. Maryland, Aug. 1993.

[21] H. V. Poor, *An Introduction to Signal Detection and Estimation Theory*. New York: Springer-Verlag.

[22] G. Swayze. (1997). "The hydrothermal and structural history of the Cuprite Mining District, Southwestern Nevada: An integrated geological and geophysical approach," Ph.D. dissertation, University of Colorado, Boulder. [Online]. Available: http://speclab.cr.usgs.gov and ftp://ftpext.cr.usgs.gov/pub/cr/co/denver/speclab/pub/cuprite/gregg.thesis.images/mineralzone.thesis.gif

[23] C.-I Chang and Q. Du, "Estimation of number of spectrally distinct signal sources in hyperspectral imagery," *IEEE Trans. Geosci. Remote Sens.*, vol. 42, no. 3, pp. 608–619, Mar. 2004.

[24] H. Ren and C.-I Chang, "Automatic spectral target recognition in hyperspectral imagery," *IEEE Trans. Aerosp. Electron. Syst.*, vol. 39, no. 4, pp. 1232–1249, Oct. 2003.

[25] C.-I Chang, W. Liu, and C.-C. Chang, "Discrimination and identification for subpixel targets in hyperspectral imagery," in *Proc. IEEE Int. Conf. Image Process.*, Singapore, Oct. 24–27, 2004, pp. 3339–3342.

[26] C.-I Chang and S.-S. Chiang, "Anomaly detection and classification for hyperspectral imagery," *IEEE Trans. Geosci. Remote Sens.*, vol. 40, no. 6, pp. 1314–1325, Jun. 2002.

[27] B. Ji, C.-I Chang, J. L. Jensen, and J. O. Jensen, "Unsupervised constrained Fisher's linear discriminant analysis," in *Proc. SPIE*, Denver, CO, Aug. 1–4, 2004, vol. 5546, pp. 344–353.

Chein-I Chang (S'86–M'87–SM'92) received the B.S. degree from Soochow University, Taipei, Taiwan, R.O.C., the M.S. degree from the Institute of Mathematics at National Tsing Hua University, Hsinchu, Taiwan, R.O.C., and the M.A. degree from the State University of New York at Stony Brook, all in mathematics. He also received the M.S. and M.S.E.E. degrees from the University of Illinois at Urbana-Champaign and the Ph.D. degree in electrical engineering from the University of Maryland, College Park, in May 1987.

He has been with the University of Maryland, Baltimore County (UMBC) since 1987 and is currently a Professor in the Department of Computer Science and Electrical Engineering. He was a Visiting Research Specialist in the Institute of Information Engineering at the National Cheng Kung University, Tainan, Taiwan, R.O.C., from 1994 to 1995. He was a Distinguished Lecture Chair at the National Chung Hsing University sponsored by the Ministry of Education in Taiwan, R.O.C., from 2005 to 2006. He is the holder of three patents and several pending on hyperspectral image processing. He is on the editorial board of the *Journal of High Speed Networks* and was the Guest Editor of a special issue of the same journal on telemedicine and applications. His research interests include multispectral/hyperspectral image processing, automatic target recognition, medical imaging, information theory and coding, signal detection and estimation, and neural networks. He has authored the book *Hyperspectral Imaging: Techniques for Spectral Detection and Classification* (New York: Kluwer, 2003).

Dr. Chang received an National Research Council (NRC) Senior Research Associateship award during 2002–2003, sponsored by the U.S. Army Soldier and Biological Chemical Command, Edgewood Chemical and Biological Center, Aberdeen Proving Ground, MD. He is an Associate Editor in the area of hyperspectral signal processing for the IEEE TRANSACTIONS ON GEOSCIENCE AND REMOTE SENSING. He is a Fellow of SPIE, and a member of Phi Kappa Phi and Eta Kappa Nu.

Baohong Ji (S'05) received the B.S. and M.S. degrees, both in computer science, from the Jilin University of Technology Changchun, China, in 1993 and 1996, respectively, and the Ph.D. degree in electrical engineering from the University of Maryland, Baltimore County, Baltimore, in 2006.

From 1997 to 2000, she served as a Lecturer in the Jilin University of Technology, China. Her research interests include remote sensing, image processing, signal processing, data compression, and pattern recognition.